Numerical analysis of electroconvection in cross-flow with unipolar charge injection

Yifei Guan [1] and Igor Novosselov [1,2,*]

[1] *Department of Mechanical Engineering, University of Washington, Seattle, Washington 98195, USA*
[2] *Institute for Nano-Engineered Systems, University of Washington, Seattle, Washington 98195, USA*

(Received 4 January 2019; published 1 October 2019; corrected 16 January 2020)

Electroconvection driven by unipolar charge injection in the presence of cross-flow between two parallel electrodes is investigated in a numerical study. The two-relaxation-time lattice Boltzmann method with a fast Poisson solver is used to resolve the spatiotemporal distribution of flow field, electric field, and charge density. Couette and Poiseuille cross-flows are applied to the solutions with established electroconvective vortices. Increasing cross-flow velocity deforms the vortices and eventually suppresses them when threshold values of velocities are reached. At intermediate flow velocities, partial suppression of the vortices leads to the reduction in electroconvection. This behavior is parameterized by a nondimensional parameter, Y—a ratio of the electrical forcing term to the viscous term in the Navier-Stokes equations. For high values of Y, the electric force dominates the flow, while for values below the critical threshold, the electric force influence is negligible and the flow is dominated by the shear.

DOI: 10.1103/PhysRevFluids.4.103701

I. INTRODUCTION

The electroconvection (EC) phenomenon was first reported by Taylor in 1966, describing cellular convection in the liquid droplet [1]. Since then, EC has been observed in a number of systems where the interaction of electrostatic force with fluids is present. In nonequilibrium electrohydrodynamic (EHD) systems [1–22], poorly conductive leaky dielectric fluids acquire unipolar charge injection at the surface interface in response to the electric field. Charge transport in the fluid can trigger instabilities, leading to the development of EC vortices [23,24]. In charge-neutral electrokinetic (EK) systems, electroconvection is triggered by the electro-osmotic slip of electrolyte in the electric double layer at membrane surfaces [25–36].

Insights into the complex multiphysics interactions are essential for understanding EK and EHD phenomena. These include (1) the electric field from the potential difference between the anode and cathode and its modifications by the space-charge effects; (2) the ion motion in the electric field; (3) the interaction between the motion of ions and the neutral molecules; and (4) the inertial and viscous forces in the complex flow. The EHD was used to describe cellular convection in deforming oil droplets under a dc electric field [1] and droplet generation in microfluidic flow and oil separation [1,24,37]. EC vortices have been observed in systems where convective transport is induced by unipolar discharge into a dielectric fluid [2–22]. The model system describing EHD electroconvection is also known as the Taylor-Melcher (TM) model. The experiment demonstrating electroconvective flow in the system with unipolar charge injection was first reported by Jolly and Melcher in 1970 [2] and by Watson *et al.* that same year [38]. Jolly and Melcher had found that the incipient cellular convection can be characterized by the electric Hartmann number $\mathrm{Ha}_e = \varepsilon E/\sqrt{\mu\sigma}$

*ivn@uw.edu

(with ε permittivity, E the applied electric field intensity, μ viscosity, and σ electric conductivity) with the assumption of uniform charge density in the fluids [2]. Watson *et al.* performed experiments on EHD stability in a space-charge-limit (SCL) current injection and found that there is a transition between SCL conduction and convection-enhanced conduction marked by increased conductivity due to the motion of the fluids [38]. Atten *et al.* have shown that for the SCL scenario $T_c = 100$, where T_c is the linear stability threshold for the electric Rayleigh number T—a ratio of electric force to viscous force [13,18,39,40]. The parameter T is also sometimes referred to as the electric Taylor number [18], thus denoted as T. The chaotic behavior of EC instabilities was investigated experimentally by Malraison and Atten, who characterized two types of power spectra of intensity fluctuations, i.e., an exponential decay when viscous force is dominant and a power-law decay when inertial force is dominant [3]. The EC coupled to heat transfer was first experimentally shown by Atten *et al.*, who observed that the Nusselt number (Nu) depends on applied electric field intensity [41]. In the annulus between concentric circular electrodes, the electric Nusselt number (Ne) trend can be described by the power-law function of electric Rayleigh number and electric Prandtl number [7,8].

The analysis of EC stability was first performed using a simplified nonlinear hydraulic model [42,43] and linear stability analysis without charge diffusion [38,44]. Atten and Moreau [45] showed that in the weak-injection limit, $C \ll 1$, where C is the charge injection level, the flow stability is determined by the criterion $T_c C^2$. In the SCL injection, $C \to \infty$, the flow stability is determined by T_c only. Nonlinear stability analysis yields $T_c = 160.75$ [46], while the experiments yield $T_c = 100$ for the same conditions [47]. Atten *et al.* suggested that the discrepancy may be due to the omission of the charge diffusion term in the analysis [46,48]. The effect of charge diffusion was investigated by Zhang *et al.* by employing linear stability analysis with a Poiseuille flow [13] and by nonlinear analysis using a multiscale method [18]. The authors found that the charge diffusion has a non-negligible effect on T_c and the transient behavior depends on the Reynolds number (Re) [13,18]. More recently, Li *et al.* performed linear analysis of the EHD-Poiseuille system and found that when the ratio of Coulomb force to viscous force increases, the transverse rolls can transition from convective instability to absolute instability [49]. Even with the inclusion of charge diffusion in the linear and nonlinear stability analysis, the predicted stability criterion T_c is always greater than the experimental value obtained by Lacroix and Atten *et al.* [46,47]. Lacroix *et al.* attributed this discrepancy to the instability associated with finite perturbation [47], suggesting that the experimental instability resulted from small perturbation (disturbance due to imperfection or error) and the theoretical solutions developed from applied finite-amplitude perturbation [47].

In the charge-neutral EK system, Rubinstein and Zaltzman showed that the electro-osmotic slip at the surface leads to instability of the double layer generating EC paired vortices, thus enhancing ion exchange at the membrane surface [25–27]. Demekhin *et al.* [50] modeled electrokinetic instability (EKI), decoupling the nonlinear Poisson-Nernst-Planck (PNP) equations and neglecting the inertial term in the Navier-Stokes equations (NSEs). Pham *et al.* [29] performed direct numerical simulation (DNS), demonstrating that the charge-neutral EKI system exhibits a hysteretic behavior in the transition between the limiting and overlimiting regimes. Kwak *et al.* [30] have examined the effect of the cross-flow on the EKI and proposed a scaling law relating the field strength and shear to the height of the vortices. More recently, Kwak *et al.* extended the scaling law analysis for the electric Nusselt number as a function of the electric Rayleigh and Reynolds numbers for the EC-induced convective ion transport [31].

The EC stability problems in both EK and EHD systems were shown to be analogous to Rayleigh-Bernard convection (RBC) [22,51–58]. Of particular interest to this work is the suppression of the RBC cells in the cross-flow [59]. The Richardson number $\mathrm{Ri} = \mathrm{Gr}/\mathrm{Re}^2$, the ratio of buoyancy to the inertia force, has been used to parametrize the effect of the applied shear, where Gr is the Grashof number. For $\mathrm{Ri} > 10$, the effect of the cross-flow is insignificant, while for $\mathrm{Ri} < 0.1$, the effect of the buoyancy can be neglected. In the EC scenario, two-dimensional (2D) finite-volume simulations of Poiseuille flow show that the critical electric Rayleigh number T_c depends on the Re

number and the ion mobility parameter M [14]. The model for the EC system is more complicated than the RBC due to the introduction of two independent variables, i.e., the charge density and electric field. With the Boussinesq approximation, the RBC system is a two-way coupling of fluid motion and heat [60]; on the other hand, EC is a three-way coupling between fluids, charge density, and electric field.

To gain insight into the complexity of the EC flow, the problem can be investigated using numerical simulations. The earlier finite-difference simulations have shown that strong numerical diffusivity may contaminate the model [4]. Other numerical approaches include the particle-in-cell method [61], finite-volume method with the flux-corrected transport scheme [62], total variation diminishing scheme [9,11,15–17], and the method of characteristics [6]. Luo *et al.* showed that a lattice Boltzmann model (LBM) could predict the linear and finite-amplitude stability criteria of the subcritical bifurcation [19–22] for both two- and three-dimensional (2D, 3D) EC flow scenarios. This unified LBM transforms the elliptic Poisson equation to a parabolic advection-diffusion equation and introduces tuning coefficients to control the evolution of the electric potential, requiring additional subiterations at each time step.

Researching the interaction between EHD-driven EC instabilities and the external flow, Castellanos *et al.* performed a linear stability analysis of Poiseuille and Couette flow under unipolar injection. The authors showed that the external flow inhibits the transverse perturbation, but the longitudinal rolls remain unaffected [63]. Lara *et al.* found that the stability of traverse rolls depends on the mobility ratio M [Eq. (9)] in the low-Reynolds-number Poiseuille flow by performing linear stability analysis [64]. The current paper investigates the numerical effects of cross-flow on EC convection in a unipolar charge injection scenario.

In this paper, we parameterize the 2D EC stability in the cross-flow between two parallel electrodes in the presence of strong unipolar injection and electric field. The segregated solver combines a two-relaxation-time (TRT) LBM modeling fluid and charged species transport and a fast Fourier transform Poisson solver to solve for the electric field directly [65]. Couette and Poiseuille cross-flow scenarios provide shear stress; the dominant terms are determined by nondimensional analysis of the governing equations. A subcritical bifurcation is characterized by the ratio of the electrical force to the viscous force.

II. GOVERNING EQUATIONS AND DIMENSIONAL ANALYSIS

The governing equations for EHD flow include the Navier-Stokes equations (NSE) with the electric forcing term $\mathbf{F_e} = -\rho_c \nabla\varphi$ in the momentum equation, the charge transport equation, and the Poisson equation for electric potential. The TM model describes cellular convection driven by unipolar charge injection for fluids with constant dielectric, and it can be parameterized in terms of nondimensional parameters [11–17,19–22,49,66]:

$$\nabla \cdot \mathbf{u} = 0, \tag{1}$$

$$\rho \frac{D\mathbf{u}}{Dt} = -\nabla P + \mu \nabla^2 \mathbf{u} - \rho_c \nabla\varphi, \tag{2}$$

$$\frac{\partial \rho_c}{\partial t} + \nabla \cdot [(\mathbf{u} - \mu_b \nabla\varphi)\rho_c - D_c \nabla \rho_c] = 0, \tag{3}$$

$$\nabla^2 \varphi = -\frac{\rho_c}{\varepsilon}, \tag{4}$$

where ρ and μ are the density and the dynamic viscosity of the working fluid, $\mathbf{u} = (u_x, u_y)$ is the velocity vector field, P is the static pressure, μ_b is the ion mobility, D_c is the ion diffusivity, ρ_c is the charge density, ε is the electric permittivity, and φ is the electric potential. The electric force provides a source term in the momentum equation [Eq. (2)] [13,67–69]. The variables to be solved are the velocity field $\mathbf{u}$, pressure P, charge density ρ_c, and electric potential φ. The flow is modeled

as periodic in the horizontal direction (x direction) and wall-bounded in the y direction. Cross-flow is applied in the x direction.

In the absence of cross-flow, the system can be nondimensionalized with the electric field properties alone [13], i.e., H is the distance between the electrodes (two plates infinite in x and y), ρ_0 is the injected charge density at the anode, and $\Delta\varphi_0$ is the voltage difference applied to the electrodes. Respectively, the time t is nondimensionalized by $H^2/(\mu_b\Delta\varphi_0)$, the velocity $\mathbf{u}$ by the ion drift velocity $u_{\text{drift}} = \mu_b\Delta\varphi_0/H$, the pressure P by $\rho_0(\mu_b\Delta\varphi_0)^2/H^2$, and the charge density in the domain ρ_c by ρ_0. Therefore, a nondimensional form of the governing equations [Eq. (1)–(4)] is

$$\nabla^* \cdot \mathbf{u}^* = 0, \tag{5}$$

$$\frac{D\mathbf{u}^*}{Dt^*} = -\nabla^* P^* + \frac{M^2}{T}\nabla^{*2}\mathbf{u}^* - CM^2\rho_c^*\nabla^*\varphi^*, \tag{6}$$

$$\frac{\partial\rho_c^*}{\partial t^*} + \nabla^* \cdot \left[(\mathbf{u}^* - \nabla^*\varphi^*)\rho_c^* - \frac{1}{Fe}\nabla^*\rho_c^*\right] = 0, \tag{7}$$

$$\nabla^{*2}\varphi^* = -C\rho_c^*, \tag{8}$$

where the asterisk denotes the nondimensional variables. These nondimensional governing equations yield four dimensionless parameters describing the system's state [9–22]:

$$M = \frac{(\varepsilon/\rho)^{1/2}}{\mu_b}, \quad T = \frac{\varepsilon\Delta\varphi_0}{\mu\mu_b}, \quad C = \frac{\rho_0 H^2}{\varepsilon\Delta\varphi_0}, \quad Fe = \frac{\mu_b\Delta\varphi_0}{D_e}. \tag{9}$$

The physical interpretations of these parameters are as follows: M is the ratio between hydrodynamic mobility and the ionic mobility, T is the ratio between electric force to the viscous force, C is the charge injection level [13,18], and Fe is the reciprocal of the charge diffusivity coefficient [13,18].

With the addition of a cross-flow, the velocity term in the nondimensional analysis of the momentum equation is modified to account for external flow $\mathbf{u}_{\text{ext}}$, while in the previous definitions [Eq. (9)] the velocity term was nondimensionalized by the drift velocity of charges $u_{\text{drift}} = \mu_b\Delta\varphi_0/H$. Here, we consider the velocity of the upper wall $\mathbf{u}_{\text{ext}} = u_{\text{wall}}\mathbf{e}_x$ in Couette flow or the centerline velocity $\mathbf{u}_{\text{ext}} = u_{\text{center}}\mathbf{e}_x$ for Poiseuille flow, where $\mathbf{e}_x$ is the x-direction unit vector. For a system with the cross-flow the governing equations become

$$\nabla^* \cdot \mathbf{u}^* = 0, \tag{10}$$

$$\frac{D\mathbf{u}^*}{Dt^*} = -\nabla^* P^* + \frac{1}{\text{Re}}\nabla^{*2}\mathbf{u}^* - X\rho_c^*\nabla^*\varphi^* + \frac{H}{\rho|\mathbf{u}_{\text{ext}}|^2}F_p, \tag{11}$$

$$\frac{\partial\rho_c^*}{\partial t^*} + \nabla^* \cdot \left[(u_{\text{ext}}^*\mathbf{u}^* - \nabla^*\varphi^*)\rho_c^* - \frac{1}{Fe}\nabla^*\rho_c^*\right] = 0, \tag{12}$$

$$\nabla^{*2}\varphi^* = -C\rho_c^*, \tag{13}$$

where $\text{Re} = \frac{\rho|\mathbf{u}_{\text{ext}}|H}{\mu}$ is the Reynolds number, $X = \frac{\rho_0\Delta\varphi_0}{\rho|\mathbf{u}_{\text{ext}}|^2}$ a ratio of electric force to inertial force [68], $u_{\text{ext}}^* = |\mathbf{u}_{\text{ext}}|/u_{\text{drift}}$ the nondimensional external velocity, and F_p is a uniform force for Poiseuille cross-flow and zero otherwise, such that $u_{\text{center}} = \frac{1}{2\mu}(\frac{H}{2})^2 F_p$. Although X was first introduced to analyze the local flow acceleration effect due to electric force [68], the parameter can also be used in global stability analysis by adopting the global variables (ρ_0 and $\Delta\varphi_0$), which has a direct analogy to Richardson number in flow with heat convection (Ri is the ratio of buoyancy to viscous shear) [59,60,70].

TABLE I. Boundary conditions for the numerical simulations.

Boundary	Macro-variable conditions	Meso-variable conditions
x Direction	Periodic	Periodic
Upper wall	$\mathbf{u} = 0$, $\varphi = 0$, and $\nabla\rho_c = 0$	LBM FBB scheme for f_i [74–78] Neumann boundary condition $\frac{\partial g_i}{\partial y} = 0$
Lower wall	$\mathbf{u} = 0$, $\varphi = \varphi_0$, and $\rho_c = \rho_0$	LBM FBB for f_i [74–78] LBM FBB for g_i [74–78]

III. RESULT AND DISCUSSION

The TRT LBM approach is used to solve the transport equations for fluid flow and charge density, coupled to a fast Poisson solver for electric potential [65]. The equilibrium state was obtained when the flow patterns became stable. The numerical code is in SI units, and the physical constants are determined by the nondimensional parameters. The numerical method is implemented in C++ using CUDA graphics processing unit (GPU) computing. The number of threads in the x direction in each GPU block is equal to NX; the number of GPU blocks in the y direction is equal to NY. Fast Fourier transform (FFT) and inverse FFT operations are performed using the CUDA FFT, or cuFFT, library [71]. All variables are computed with double precision to reduce truncation errors. The numerical method was shown to be second-order accurate in space. Error analysis is provided in the Supplemental Materials [72]. To reduce computational cost while maintaining accuracy, the grid of $NX = 122$, $NY = 100$ is used throughout this work. The macroscopic and mesoscopic boundary conditions are specified in Table I. The no-slip boundary conditions are applied at both electrodes for fluid flow. A constant charge density at the anode (lower wall) represents a unipolar injection; a zero-diffusive flux condition $\nabla\rho_c = 0$ at the cathode (upper wall) represents an outflow current. A constant electric potential is applied at the anode; the cathode is grounded ($\varphi = 0$). At mesoscale, the discrete distribution function of velocity $f_i(\mathbf{x}, t)$ and charge density $g_i(\mathbf{x}, t)$ are used. The details on the transformations between macrovariables ($\mathbf{u}$, ρ_c) and mesovariables (f_i, g_i) are presented in the Supplemental Materials [72] and can be found in our recent publication [65]. The LBM full-way bounce-back (FBB) scheme is used for the Dirichlet (no-slip) boundary conditions for the fluid flow [19,20,73] and for charge density at the lower wall. The g_i Neumann boundary condition is set as a current outlet boundary condition for charge density transport [19,20,74].

For the hydrostatic-based state the numerical solutions of electric field and charge density agree with the model of Luo *et al.* [19,20] and the analytical solution based on a reduced set of equations for the electric field in one-dimensional coordinates [61,69], see Fig. 1. This comparison acts as a

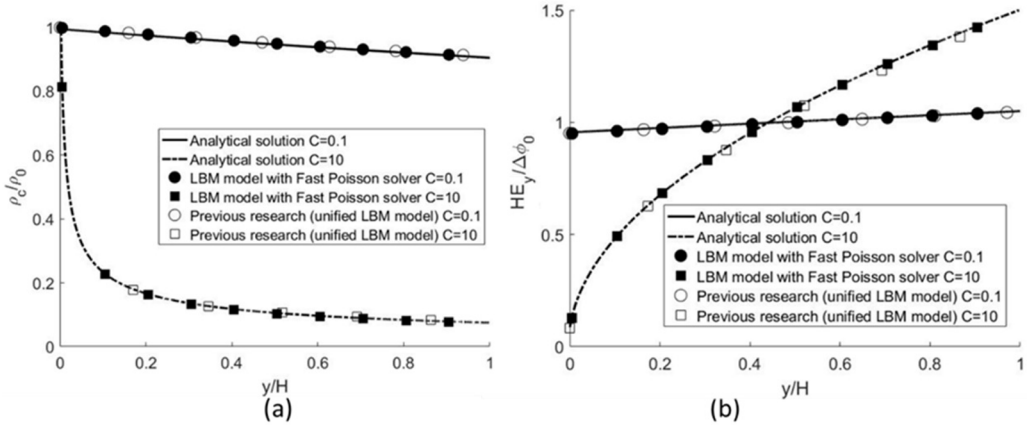

FIG. 1. Hydrostatic solution comparison of the TRT LBM and fast Poisson solver [65], unified SRT LBM [19], and the analytical solution [61,69] for $C = 0.1$ and $C = 10$, $Fe = 4000$: (a) charge density and (b) electric field.

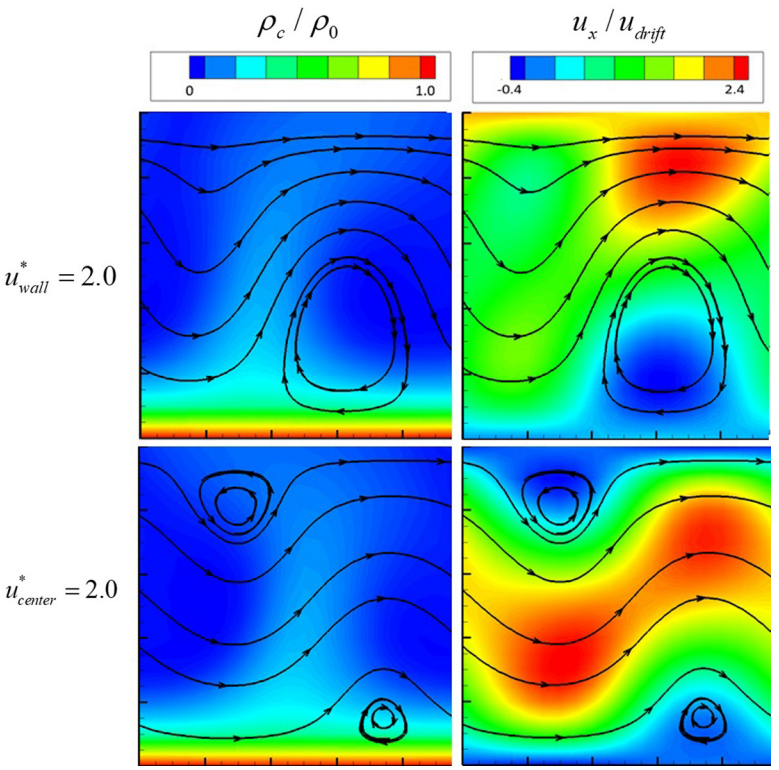

FIG. 2. Charge density and x-direction velocity color contours of the EC with cross-flow. Top: Couette flow with $u^*_{\text{wall}} = 2.0$; one of the two vortices is suppressed. Bottom: Poiseuille flow with $u^*_{\text{center}} = 2.0$; both vortices are suppressed and displaced towards the walls.

validation of the numerical method:

$$\rho_c = \rho_a (y + y_a)^{-1/2}, \tag{14}$$

$$E_y = \frac{2\rho_a}{\varepsilon}\left(y + y_a\right)^{1/2}, \tag{15}$$

where ρ_a and y_a are two-dimensional parameters which depend on the boundary conditions and geometry. At the hydrostatic-based state, the parameters C and Fe dominate the system. Figure 1 shows the profiles of normalized charge density and electric field for $C = 0.1$ and $C = 10$ with $Fe = 4000$. A more detailed description of the analytical solution is included in the Supplemental Material [72].

To model EC vortices, the hydrostatic base state is perturbed using a finite-amplitude wave-form function that satisfies the boundary conditions and continuity equation:

$$\begin{aligned} u_x &= L_x \sin(2\pi y/L_y)\sin(2\pi x/L_x) \times \varepsilon \\ u_y &= L_y[\cos(2\pi y/L_y) - 1]\cos(2\pi x/L_x) \times \varepsilon. \end{aligned} \tag{16}$$

The physical domain size $Lx = 1.22m$ and $Ly = 1m$ limits the perturbation wave number to $\lambda_x = 2\pi/L_x \approx 5.15(1/m)$, yielding the most unstable mode under the conditions $C = 10$, $M = 10$, and $Fe = 4000$ [20]. The perturbation magnitude, $\varepsilon = 10^{-3}$, is small enough to not affect the flow structures within the linear growth region [65]. The electric Nusselt number, $\text{Ne} = I/I_0$, serves as a flow stability criteria, where I is the cathode current for a given solution and I_0 is the cathode current for the hydrostatic solution [9,20]; thus if the EC vortices exist, $\text{Ne} > 1$. In

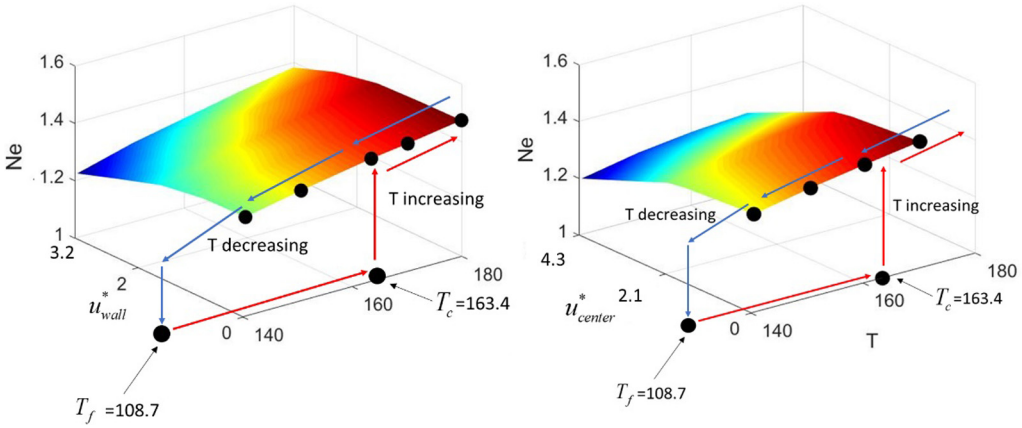

FIG. 3. Electric Nusselt number as a function of the electric Rayleigh number T and (a) applied velocity of the upper wall u^*_{wall} for Couette-type cross-flow or (b) applied body force F_p represented by the centerline velocity u^*_{center} for Poiseuille-type cross-flow. Partial suppression of the EC vortices leads to the reduction in electroconvection for the entire range of electric Rayleigh number.

the cases with strong ion injection, the EC stability largely depends on T, so in this analysis, T is varied while other nondimensional parameters are held constant at $C = 10$, $M = 10$, and $Fe = 4000$.

Couette cross-flow is added to the simulation with the established EC vortices by assigning a constant upper wall velocity. To model Poiseuille flow, a body force in the x direction is added. Figure 2 shows the charge density and x-direction velocity for intermediate cross-flow strength Couette cross-flow ($u^*_{\text{wall}} = 2.0$) and Poiseuille cross-flow ($u^*_{\text{center}} = 2.0$) at $T = 170.07$. The Couette cross-flow stretches the vortices in the direction of the bulk flow, eliminating one of the two vortices. In a Poiseuille cross-flow, the vortex pair becomes separated; the vortices are pushed toward the opposite walls. With the increasing cross-flow, both vortices are eliminated and $I = I_0$, Ne = 1(see Fig. 6). The EC contribution to the flow field is negligible at higher values of shear stress (higher velocity), and the flow field becomes identical to the cross-flow without charge injection.

Figure 3 shows the extended stability analysis of EC without cross-flow [65] by introducing (a) finite velocity of the upper wall (cathode) and (b) a uniform body force for pressure-driven flow F_p. For a constant T, Ne decreases as u^*_{wall} or u^*_{center} increases. Figure 3 shows that in the cases without cross-flow, a hysteresis loop is observed for Ne as a function of T, which is consistent with previous theoretical studies [13,18], experimental results [46], and numerical simulations [11,15,17,19,20,65]. The shape of the Ne vs T plot in cases with cross-flow is similar. However, the magnitude of Ne is lower; thus the convective charge transport (and the current) are reduced when the cross-flow is applied due to the partial suppression of the EC vortices.

Figures 4(a) and 4(b) show that Ne decreases as Re increases (stronger cross-flow), which agrees with the observation that cross-flow suppresses EC vortices and stabilizes the system. As previously shown, the intensity of convection strongly depends on T when cross-flow is not present [65]. Figure 3 shows that when cross-flow is present and while holding C, M, and Fe constant, $\text{Ne} = f_1(T, u^*_{\text{ext}})$. To gain insight into the vortices and the cross-flow interaction, it is convenient to plot Ne vs nondimensional groups that contain the velocity term. The analysis can be aided by taking a nondimensional curl ($\nabla^* \times$) of Eq. (6) for $u^*_{\text{ext}} = 0$ and Eq. (11)

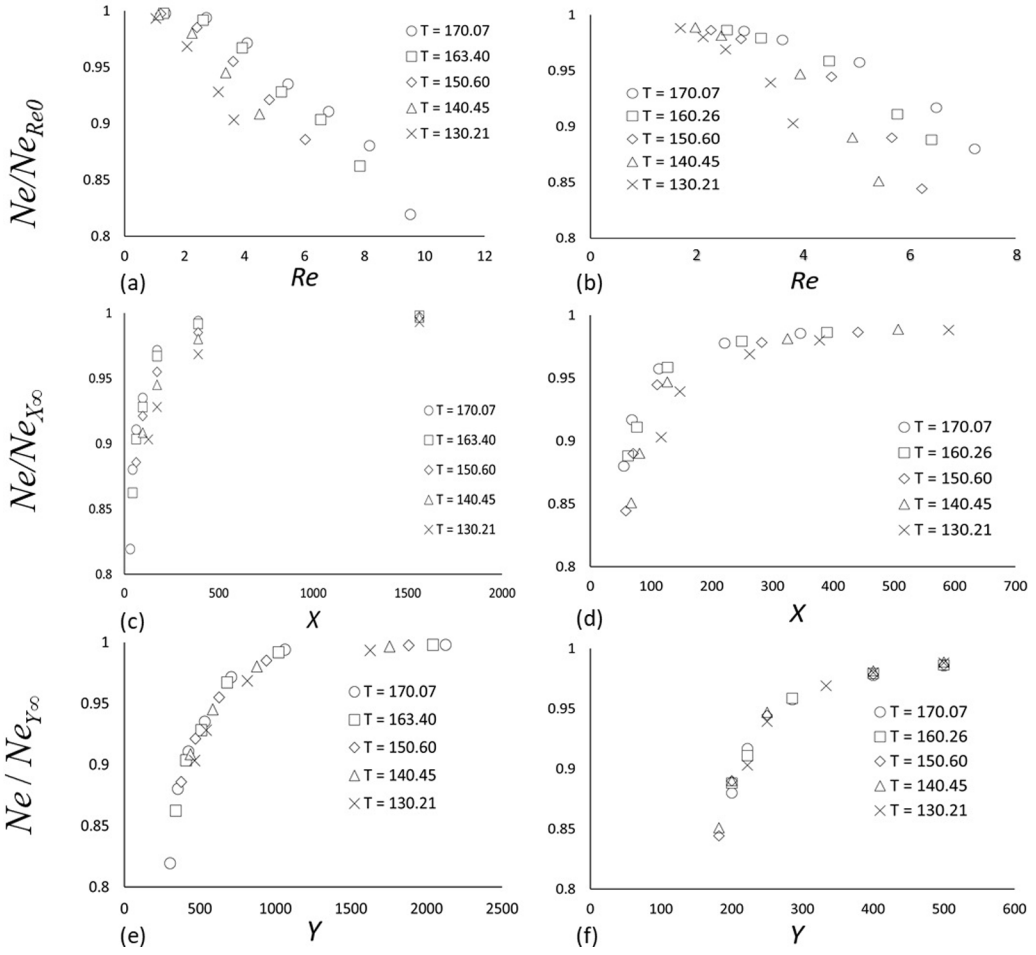

FIG. 4. Electric Nusselt vs nondimensional parameters. (a), (c), (e) Couette cross-flow is applied. (b), (d), (f) Poiseuille-type cross-flow is applied. (a), (b) $\mathrm{Ne}/\mathrm{Ne}_{\mathrm{Re0}}$ vs Re showing that the flow becomes more stable for increasing Re or cross-flow. (c), (d) $\mathrm{Ne}/\mathrm{Ne}_{X\infty}$ vs X. (e), (f) $\mathrm{Ne}/\mathrm{Ne}_{Y\infty}$ collapses on a single curve for various T and Y indicating that $\mathrm{Ne}/\mathrm{Ne}_{Y\infty}$ is a function of Y only for constant C. $\mathrm{Ne}_{Re0} = \mathrm{Ne}_{X\infty} = \mathrm{Ne}_{Y\infty}$ is the electric Nusselt number without cross-flow.

for $u^*_{\mathrm{ext}} \neq 0$:

$$\frac{D\omega^*}{Dt^*} = \frac{M^2}{T}\nabla^{*2}\omega^* - CM^2(\nabla^*\rho_c^* \times \nabla^*\varphi^*), \tag{17}$$

$$\frac{D\omega^*}{Dt^*} = \frac{1}{\mathrm{Re}}\nabla^{*2}\omega^* - X(\nabla^*\rho_c^* \times \nabla^*\varphi^*), \tag{18}$$

where ω^* is the nondimensional vorticity, which is a scalar in the 2D flow. The two terms on the right-hand side of Eqs. (17) and (18) are significant with respect to growth or decay of the vortices. Figures 4(a)–4(d) show that Re and X cannot serve as similarity parameters that describe the behavior of the system. However, if Ne is plotted against the product of Re and X (defined as Y), the $\mathrm{Ne} = f_1(T, u^*_{\mathrm{ext}})$ collapses on a single curve, see Figs. 4(e) and 4(f). Here Ne is normalized by $\mathrm{Ne}_{\mathrm{Re0}}$, $\mathrm{Ne}_{X\infty}$, or $\mathrm{Ne}_{Y\infty}$, which are the solutions without cross-flow $\mathrm{Re} \to 0$, $X \to \infty$, $Y \to \infty$ [65]. The physical interpretation of Y is as follows. Since Re is the ratio of inertia to viscous force and X is

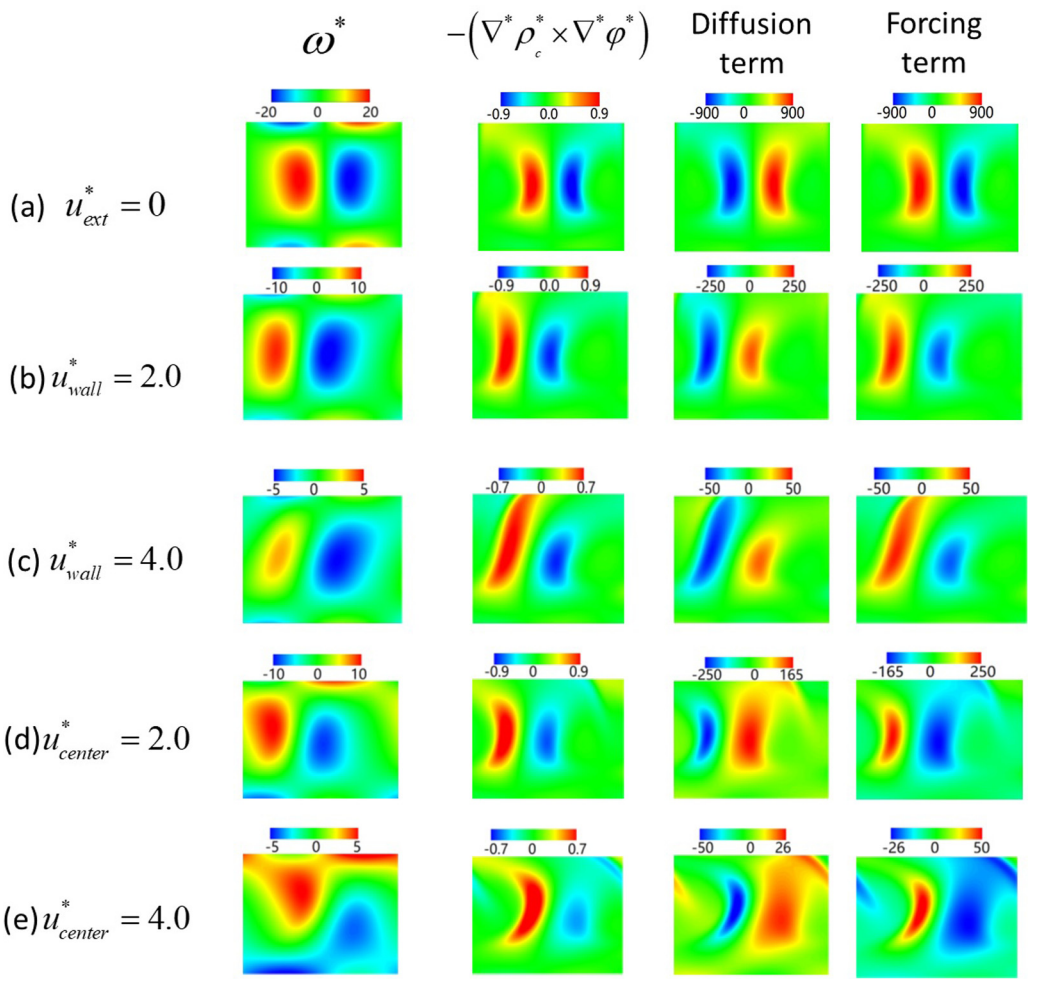

FIG. 5. Color contours of vorticity ω^*, curl of electric force $-(\nabla^*\rho_c^*\times\nabla^*\varphi^*)$, diffusion and forcing terms from Eqs. (17) and (18), with and without cross-flow: (a) no cross-flow, both vortices exist; (b) intermediate Couette flow with $u^*_{\text{wall}}=2.0$, one of the two vortices is suppressed. (c) strong Couette flow with $u^*_{\text{wall}}=4.0$; (d) intermediate Poiseuille flow $u^*_{\text{center}}=2.0$, vortices are suppressed and displaced towards the walls; and (e) strong Poiseuille flow with $u^*_{\text{center}}=4.0$.

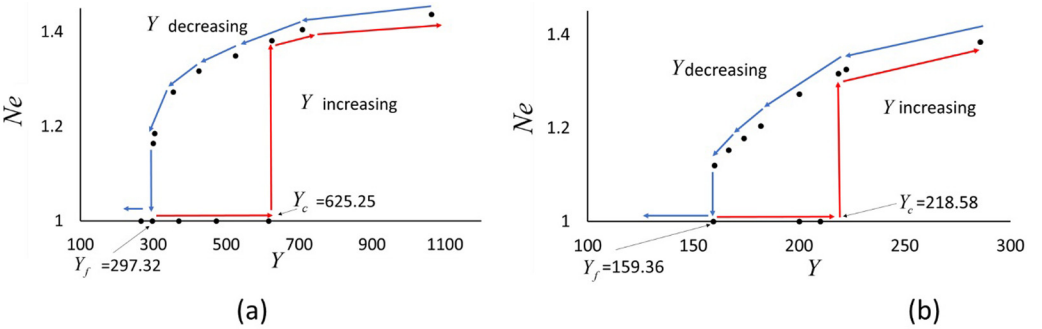

FIG. 6. Electrical Nusselt number Ne vs *Y*. Bifurcation thresholds are (a) Couette cross-flow $Y_c=625.25$ and $Y_f=297.32$, and (b) Poiseuille cross-flow $Y_f=159.36$ and $Y_c=218.58$.

the ratio of electric force to inertia, their product is the ratio of electric force to viscous force:

$$Y = X \times \mathrm{Re} = \frac{\rho_0 \Delta\varphi_0 H}{\mu |\mathbf{u}_{\mathrm{ext}}|} = \frac{\rho_0 \Delta\varphi_0}{|\tau|}, \tag{19}$$

where τ is the shear stress. In Couette flow, $\tau = constant$; in Poiseuille flow, the average value for the channel flow is used. In terms of nondimensional parameters M, C, T, and u^*_{ext}, $X = CM^2/(u^*_{\mathrm{ext}})^2$ and $Y = CT/u^*_{\mathrm{ext}}$. When the cross-flow is not present, $\mathrm{Ne}_{\mathrm{Re}0} = \mathrm{Ne}_{X\infty} = \mathrm{Ne}_{Y\infty} = f_2(T)$ [19,20,65]. Since $\mathrm{Ne}/\mathrm{Ne}_{Y\infty}(T)$ collapses on the same curve when plotted against Y, the EC stability in cross-flow can be parameterized by a single nondimensional parameter, which is inversely proportional to τ. In other words, $\mathrm{Ne}/\mathrm{Ne}_{Y\infty} = f_1(T, u^*_{\mathrm{ext}})/f_2(T) = f_3(T/u^*_{\mathrm{ext}})$ for constant C, M, and Fe, [$f_i(\cdot)$, $i = 1, 2, 3$ denotes a function of]. As the $Y = CT/u^*_{\mathrm{ext}}$ for $C = \mathrm{const}$, $\mathrm{Ne}/\mathrm{Ne}_{Y\infty} = f_3(T/u^*_{\mathrm{ext}}) = f_3(Y)$. Figure 4 shows the solutions with the established EC vortices, which represents the upper bifurcation branch with $\mathrm{Ne} > 1$ (as shown in Fig. 6).

Figure 5 shows the effects of intermediate and strong cross-flow on vorticity ω^* and curl of electric force $-(\nabla^*\rho_c^* \times \nabla^*\varphi^*)$, the diffusion term $\frac{M^2}{T}\nabla^{*2}\omega^*$ as in Eq. (17) without cross-flow or $\frac{1}{\mathrm{Re}}\nabla^{*2}\omega^*$ as in Eq. (18) with cross-flow, and the forcing term $-CM^2(\nabla^*\rho_c^* \times \nabla^*\varphi^*)$ as in Eq. (17) without cross-flow or $-X(\nabla^*\rho_c^* \times \nabla^*\varphi^*)$ as in Eq. (18) with cross-flow. As expected, maximum and minimum values of vorticity correlate with the maximum and minimum values of the curl of electric force and forcing term, see Eqs. (17) and (18), implying that the Coulombic forcing term leads to vorticity generation. When an intermediate cross-flow is applied [Figs. 5(b) and 5(d)], the symmetry of the vortex pair is disrupted and the curl of the electric force is also asymmetric. For strong cross-flow [Figs. 5(c) and 5(e)], the magnitude forcing term is lower, leading to lower vorticity generation. One of the most significant findings in this analysis is that the reduction in the forcing term $X(\nabla^*\rho_c^* \times \nabla^*\varphi^*)$ does not come from the expression $(\nabla^*\rho_c^* \times \nabla^*\varphi^*)$ but rather from X, as seen by comparing Fig. 5 (columns 2 and 4). Thus variations in values of X are responsible for the changes in vorticity generation.

On the other hand, it is apparent from Fig. 5 that the diffusion balances the forcing term; for all cases, the diffusion terms have equal and opposite values of the forcing terms over the wide range of values, while the vorticity magnitudes do not change significantly. Similarly to the forcing, the diffusion term in Eq. (18) is the product of two nondimensional groups: 1/Re and $\nabla^{*2}\omega^*$. Figure 4 shows that Re changes by order of magnitude acting as a scaling factor in the diffusion term Eq. (18). Multiplication of both diffusion and forcing terms by Re yields a coefficient of unity in diffusion term and parameter Y in the forcing term.

To examine hysteresis associated with the formation and suppression of EC vortices, Fig. 6 shows the $\mathrm{Ne} = f(Y)$ for fixed $C = 10$, $M = 10$, $T = 170.07$, and $Fe = 4000$. Both Couette and Poiseuille cross-flows are examined. A hysteresis loop with subcritical bifurcation is observed; the bifurcation thresholds are $Y_c = 625.25$, $Y_f = 297.32$ for Couette flow and $Y_c = 218.58$, $Y_f = 159.36$ for Poiseuille flow. The critical values of Y_c correspond to $\mathrm{Re}_c \sim O(1)$ ($\mathrm{Re}_c = 4.63$ for Couette flow and $\mathrm{Re}_c = 2.94$ for Poiseuille flow), which is consistent with linear stability analysis [64] for $T = 170.07$. Similar to stability parameter T for $\mathrm{Re} = 0$ (Fig. 3), for $Y < Y_c$, the system does not yield the EC instability, returning to the unperturbed state ($I = I_0$ and $\mathrm{Ne} = 1$). If Y decreases after the EC vortices are formed, Ne decreases nonlinearly, until $Y = Y_f$, then the EC vortices are suppressed; the flow is not influenced by the electric forces.

The results presented in this work consider the interaction cross-flow electroconvective transport due to the unipolar charge injection; the presented methodology can be extended to more complex convective systems such as RBC and charge-neutral electrokinetic systems. The 2D case in this work can be regarded as a special case in the 3D flow scenario, i.e., the traverse rolling pattern [19,20]. Multimodal 3D structures (square patterns, hexagonal patterns, and mixed patterns) are ubiquitous in convective flows such as in EKI [58], EHD [20,21,79], and RBC [51,52,59,80–83]. The effect of cross-flow has been observed in all three scenarios; the summary and the analogy to EKI and RBC is shown in Table II.

TABLE II. Nondimensional parameter analogy for RBC and EHD electroconvection in the presence of cross-flow velocity $\mathbf{u}_{\text{ext}}$.

Physical interpretation	Electrohydrodynamic convection (EHD)		Heat convection (RBC)
	As presented here (including charge density)	Based on average field properties (without charge density)	
$\frac{\text{Body force}}{\text{Inertial force}}$	$X = \frac{\rho_0 \Delta\varphi_0}{\rho \lvert\mathbf{u}_{\text{ext}}\rvert^2}$ [68]	$N_{ei} = \frac{\varepsilon \Delta\varphi_0^2}{\rho H^2 \lvert\mathbf{u}_{\text{ext}}\rvert^2}$ [84,85]	$\text{Ri} = \text{Gr}/\text{Re}^2 = \frac{g' H}{\lvert\mathbf{u}_{\text{ext}}\rvert^2}$ [59]
$\frac{\text{Body force}}{\text{Viscous force}}$	$Y = X \times \text{Re} = \frac{\rho_0 \Delta\varphi_0}{\lvert\tau\rvert}$	$N_{ev} = N_{ei} \times \text{Re} = \frac{\varepsilon \Delta\varphi_0^2}{\mu H \lvert\mathbf{u}_{\text{ext}}\rvert}$ [84,85]	$\text{Gr}/\text{Re} = \frac{g' \rho H^2}{\mu \lvert\mathbf{u}_{\text{ext}}\rvert}$

where $g' = g\frac{\Delta\rho}{\rho}$ is the reduced gravity [60]. In the context of EKI, the convection can also be characterized by nondimensional parameters such as electric Nusselt number, electric Rayleigh number, and Reynolds number [30,31].

IV. CONCLUSION

The 2D numerical study extends the EC stability analysis to Couette and Poiseuille flows between two infinitely long parallel electrodes with unipolar charge injection. The numerical approach utilizes the two-relaxation-time LBM to solve the flow and charge transport equations and a fast Poisson solver to solve the Poisson equation. Increasing cross-flow velocity deforms the vortices and eventually suppresses them when threshold values of velocities are reached. Partial suppression of the vortices leads to a reduction in electroconvection for the entire range of the electric Rayleigh number. The nondimensional analysis of the governing equations is used to derive the parameter Y, a ratio of electric force to viscous force, in the presence of cross-flow. The nondimensional parameter Y accounts for the effect of the shear stress, analogous to the Richardson number Ri, (the ratio of buoyancy to the inertial forces), which is used to parametrize the effect of the applied shear in RBC. Similar to the stability parameter T for the hydrostatic case, a hysteresis loop with subcritical bifurcation is observed. For $C = 10$, $M = 10$, $T = 170.07$, and $Fe = 4000$, the bifurcation thresholds are $Y_c = 625.25$, $Y_f = 297.32$ for Couette flow and $Y_c = 218.58$, $Y_f = 159.36$ for Poiseuille flow.

ACKNOWLEDGMENTS

This research was supported by the DHS Science and Technology Directorate and the UK Home Office, Grant No. HSHQDC-15-531 C-B0033, and by the National Institutes of Health, Grant No. NIBIB U01 EB021923.

[1] G. I. Taylor, Studies in Electrohydrodynamics, I. The circulation produced in a drop by an electric field, Proc. R. Soc. London, Ser. A **291**, 159 (1966).

[2] D. C. Jolly and J. R. Melcher, Electroconvective instability in a fluid layer, Proc. R. Soc. London, Ser. A **314**, 269 (1970).

[3] B. Malraison and P. Atten, Chaotic Behavior of Instability Due to Unipolar Ion Injection in a Dielectric Liquid, Phys. Rev. Lett. **49**, 723 (1982).

[4] A. Castellanos and P. Atten, Numerical modeling of finite amplitude convection of liquids subjected to unipolar injection, IEEE Trans. Ind. Appl. **IA-23**, 825 (1987).

[5] Z. A. Daya, V. B. Deyirmenjian, and S. W. Morris, Bifurcations in annular electroconvection with an imposed shear, Phys. Rev. E **64**, 036212 (2001).
[6] K. Adamiak and P. Atten, Simulation of corona discharge in point–plane configuration, J. Electrostat. **61**, 85 (2004).
[7] P. Tsai, Z. A. Daya, and S. W. Morris, Aspect-Ratio Dependence of Charge Transport in Turbulent Electroconvection, Phys. Rev. Lett. **92**, 084503 (2004).
[8] P. Tsai, Z. A. Daya, and S. W. Morris, Charge transport scaling in turbulent electroconvection, Phys. Rev. E **72**, 046311 (2005).
[9] P. Traoré and A. Pérez, Two-dimensional numerical analysis of electroconvection in a dielectric liquid subjected to strong unipolar injection, Phys. Fluids **24**, 037102 (2012).
[10] P. Traoré and J. Wu, On the limitation of imposed velocity field strategy for Coulomb-driven electroconvection flow simulations, J. Fluid Mech. **727**, R3 (2013).
[11] J. Wu, P. Traoré, P. A. Vázquez, and A. T. Pérez, Onset of convection in a finite two-dimensional container due to unipolar injection of ions, Phys. Rev. E **88**, 053018 (2013).
[12] A. Pérez, P. Vázquez, J. Wu, and P. Traoré, Electrohydrodynamic linear stability analysis of dielectric liquids subjected to unipolar injection in a rectangular enclosure with rigid sidewalls, J. Fluid Mech. **758**, 586 (2014).
[13] M. Zhang, F. Martinelli, J. Wu, P. J. Schmid, and M. Quadrio, Modal and non-modal stability analysis of electrohydrodynamic flow with and without cross-flow, J. Fluid Mech. **770**, 319 (2015).
[14] P. Traore, J. Wu, C. Louste, P. A. Vazquez, and A. T. Perez, Numerical study of a plane Poiseuille channel flow of a dielectric liquid subjected to unipolar injection, IEEE Trans. Dielectr. Electr. Insul. **22**, 2779 (2015).
[15] J. Wu and P. Traoré, A finite-volume method for electro-thermoconvective phenomena in a plane layer of dielectric liquid, Numer. Heat Transfer, Part A **68**, 471 (2015).
[16] J. Wu, A. T. Perez, P. Traore, and P. A. Vazquez, Complex flow patterns at the onset of annular electroconvection in a dielectric liquid subjected to an arbitrary unipolar injection, IEEE Trans. Dielectr. Electr. Insul. **22**, 2637 (2015).
[17] J. Wu, P. Traoré, A. T. Pérez, and P. A. Vázquez, On two-dimensional finite amplitude electro-convection in a dielectric liquid induced by a strong unipolar injection, J. Electrostat. **74**, 85 (2015).
[18] M. Zhang, Weakly nonlinear stability analysis of subcritical electrohydrodynamic flow subject to strong unipolar injection, J. Fluid Mech. **792**, 328 (2016).
[19] K. Luo, J. Wu, H.-L. Yi, and H.-P. Tan, Lattice Boltzmann model for Coulomb-driven flows in dielectric liquids, Phys. Rev. E **93**, 023309 (2016).
[20] K. Luo, J. Wu, H.-L. Yi, and H.-P. Tan, Three-dimensional finite amplitude electroconvection in dielectric liquids, Phys. Fluids **30**, 023602 (2018).
[21] K. Luo, J. Wu, H.-L. Yi, L.-H. Liu, and H.-P. Tan, Hexagonal convection patterns and their evolutionary scenarios in electroconvection induced by a strong unipolar injection, Phys. Rev. Fluids **3**, 053702 (2018).
[22] K. Luo, T.-F. Li, J. Wu, H.-L. Yi, and H.-P. Tan, Mesoscopic simulation of electrohydrodynamic effects on laminar natural convection of a dielectric liquid in a cubic cavity, Phys. Fluids **30**, 103601 (2018).
[23] M. Z. Bazant, Electrokinetics meets electrohydrodynamics, J. Fluid Mech. **782**, 1 (2015).
[24] Y. Mori and Y.-N. Young, From electrodiffusion theory to the electrohydrodynamics of leaky dielectrics through the weak electrolyte limit, J. Fluid Mech. **855**, 67 (2018).
[25] I. Rubinstein and B. Zaltzman, Electro-osmotically induced convection at a permselective membrane, Phys. Rev. E **62**, 2238 (2000).
[26] I. Rubinstein and B. Zaltzman, Electro-osmotic slip of the second kind and instability in concentration polarization at electrodialysis membranes, Math. Models Methods Appl. Sci. **11**, 263 (2001).
[27] B. Zaltzman and I. Rubinstein, Electro-osmotic slip and electroconvective instability, J. Fluid Mech. **579**, 173 (2007).
[28] S. M. Rubinstein, G. Manukyan, A. Staicu, I. Rubinstein, B. Zaltzman, R. G. Lammertink, F. Mugele, and M. Wessling, Direct Observation of a Nonequilibrium Electro-Osmotic Instability, Phys. Rev. Lett. **101**, 236101 (2008).

[29] V. S. Pham, Z. Li, K. M. Lim, J. K. White, and J. Han, Direct numerical simulation of electroconvective instability and hysteretic current-voltage response of a permselective membrane, Phys. Rev. E **86**, 046310 (2012).
[30] R. Kwak, V. S. Pham, K. M. Lim, and J. Han, Shear Flow of an Electrically Charged Fluid by Ion Concentration Polarization: Scaling Laws for Electroconvective Vortices, Phys. Rev. Lett. **110**, 114501 (2013).
[31] R. Kwak, V. S. Pham, and J. Han, Sheltering the perturbed vortical layer of electroconvection under shear flow, J. Fluid Mech. **813**, 799 (2017).
[32] C. Druzgalski, M. Andersen, and A. Mani, Direct numerical simulation of electroconvective instability and hydrodynamic chaos near an ion-selective surface, Phys. Fluids **25**, 110804 (2013).
[33] S. M. Davidson, M. B. Andersen, and A. Mani, Chaotic Induced-Charge Electro-Osmosis, Phys. Rev. Lett. **112**, 128302 (2014).
[34] S. M. Davidson, M. Wessling, and A. Mani, On the dynamical regimes of pattern-accelerated electroconvection, Sci. Rep. **6**, 22505 (2016).
[35] I. Rubinstein and B. Zaltzman, Convective diffusive mixing in concentration polarization: From Taylor dispersion to surface convection, J. Fluid Mech. **728**, 239 (2013).
[36] I. Rubinstein and B. Zaltzman, Equilibrium Electroconvective Instability, Phys. Rev. Lett. **114**, 114502 (2015).
[37] D. Saville, Electrohydrodynamics: The Taylor-Melcher leaky dielectric model, Annu. Rev. Fluid Mech. **29**, 27 (1997).
[38] P. Watson, J. Schneider, and H. Till, Electrohydrodynamic Stability of Space-Charge-Limited Currents in Dielectric Liquids, II. Experimental Study, Phys. Fluids **13**, 1955 (1970).
[39] K. Luo, A. T. Pérez, J. Wu, H.-L. Yi, and H.-P. Tan, Efficient lattice Boltzmann method for electrohydrodynamic solid-liquid phase change, Phys. Rev. E **100**, 013306 (2019).
[40] K. Luo, J. Wu, A. T. Pérez, H.-L. Yi, and H.-P. Tan, Stability analysis of electroconvection with a solid-liquid interface via the lattice Boltzmann method, Phys. Rev. Fluids **4**, 083702 (2019).
[41] P. Atten, F. McCluskey, and A. Perez, Electroconvection and its effect on heat transfer, IEEE Trans. Electr. Insul. **23**, 659 (1988).
[42] N. Felici, Phénomenes hydro et aérodynamiques dans la conduction des diélectriques fluides, Rev. Gén. Electr. **78**, 717 (1969).
[43] N. Felici and J. Lacroix, Electroconvection in insulating liquids with special reference to uni-and bi-polar injection: a review of the research work at the CNRS Laboratory for Electrostatics, Grenoble 1969–1976, J. Electrostat. **5**, 135 (1978).
[44] J. Schneider and P. Watson, Electrohydrodynamic stability of space-charge-limited currents in dielectric liquids. I. Theoretical study, Phys. Fluids **13**, 1948 (1970).
[45] P. Atten and R. Moreau, Stabilité électrohydrodynamique des liquides isolants soumis à une injection unipolaire, J. Mécanique **11**, 471 (1972).
[46] P. Atten and J. Lacroix, Non-linear hydrodynamic stability of liquids subjected to unipolar injection, J. Mécanique **18**, 469 (1979).
[47] J. Lacroix, P. Atten, and E. Hopfinger, Electro-convection in a dielectric liquid layer subjected to unipolar injection, J. Fluid Mech. **69**, 539 (1975).
[48] P. Atten, Rôle de la diffusion dans le problème de la stabilité hydrodynamique d'un liquide dièlectrique soumis à une injection unipolaire forte, CR Acad. Sci. Paris **283**, 29 (1976).
[49] F. Li, B.-F. Wang, Z.-H. Wan, J. Wu, and M. Zhang, Absolute and convective instabilities in electrohydrodynamic flow subjected to a Poiseuille flow: A linear analysis, J. Fluid Mech. **862**, 816 (2019).
[50] E. Demekhin, V. Shelistov, and S. Polyanskikh, Linear and nonlinear evolution and diffusion layer selection in electrokinetic instability, Phys. Rev. E **84**, 036318 (2011).
[51] S. Chandrasekhar, *Hydrodynamic and Hydromagnetic Stability* (Courier Corporation, North Chelmsford, MA, 2013).
[52] P. G. Drazin and W. H. Reid, *Hydrodynamic Stability* (Cambridge University Press, Cambridge, England, 2004).

[53] E. L. Koschmieder, *Bénard Cells and Taylor Vortices* (Cambridge University Press, Cambridge, England, 1993).
[54] P. Bergé and M. Dubois, Rayleigh-Bénard convection, Contemp. Phys. **25**, 535 (1984).
[55] M. Krishnan, V. M. Ugaz, and M. A. Burns, PCR in a Rayleigh-Benard convection cell, Science **298**, 793 (2002).
[56] A. V. Getling, *Rayleigh-Benard Convection: Structures and Dynamics* (World Scientific, Singapore, 1998), Vol. 11.
[57] E. Demekhin, N. Nikitin, and V. Shelistov, Direct numerical simulation of electrokinetic instability and transition to chaotic motion, Phys. Fluids **25**, 122001 (2013).
[58] E. Demekhin, N. Nikitin, and V. Shelistov, Three-dimensional coherent structures of electrokinetic instability, Phys. Rev. E **90**, 013031 (2014).
[59] A. Mohamad and R. Viskanta, Laminar flow and heat transfer in Rayleigh-Benard convection with shear, Phys. Fluids A **4**, 2131 (1992).
[60] J. S. Turner, *Buoyancy Effects in Fluids* (Cambridge University Press, Cambridge, England, 1979).
[61] R. Chicón, A. Castellanos, and E. Martin, Numerical modelling of Coulomb-driven convection in insulating liquids, J. Fluid Mech. **344**, 43 (1997).
[62] P. Vazquez, G. Georghiou, and A. Castellanos, Characterization of injection instabilities in electrohydrodynamics by numerical modelling: Comparison of particle in cell and flux corrected transport methods for electroconvection between two plates, J. Phys. D Appl. Phys. **39**, 2754 (2006).
[63] A. Castellanos and N. Agrait, Unipolar injection induced instabilities in plane parallel flows, IEEE Trans. Ind. Appl. **28**, 513 (1992).
[64] J. L. Lara, A. Castellanos, and F. Pontiga, Destabilization of plane Poiseuille flow of insulating liquids by unipolar charge injection, Phys. Fluids **9**, 399 (1997).
[65] Y. Guan and I. Novosselov, Two relaxation time lattice Boltzmann method coupled to fast Fourier transform Poisson solver: Application to electroconvective flow, J. Comput. Phys. **397**, 108830 (2019).
[66] J. Wu, P. Traoré, M. Zhang, A. T. Pérez, and P. A. Vázquez, Charge injection enhanced natural convection heat transfer in horizontal concentric annuli filled with a dielectric liquid, Int. J. Heat Mass Transfer **92**, 139 (2016).
[67] Y. Zhang, L. Liu, Y. Chen, and J. Ouyang, Characteristics of ionic wind in needle-to-ring corona discharge, J. Electrostat. **74**, 15 (2015).
[68] Y. Guan, R. S. Vaddi, A. Aliseda, and I. Novosselov, Experimental and numerical investigation of electrohydrodynamic flow in a point-to-ring corona discharge, Phys. Rev. Fluids **3**, 043701 (2018).
[69] Y. Guan, R. S. Vaddi, A. Aliseda, and I. Novosselov, Analytical model of electro-hydrodynamic flow in corona discharge, Phys. Plasmas **25**, 083507 (2018).
[70] H. D. Abarbanel, D. D. Holm, J. E. Marsden, and T. Ratiu, Richardson Number Criterion for the Nonlinear Stability of Three-Dimensional Stratified Flow, Phys. Rev. Lett. **52**, 2352 (1984).
[71] N. Goodnight, CUDA/OpenGL fluid simulation, NVIDIA Corporation, April 2007.
[72] See Supplemental Material at http://link.aps.org/supplemental/10.1103/PhysRevFluids.4.103701 for the analytical solutions, LBM scheme details, and error analysis.
[73] I. Ginzbourg and P. Adler, Boundary flow condition analysis for the three-dimensional lattice Boltzmann model, J. Phys. II **4**, 191 (1994).
[74] T. Krüger, H. Kusumaatmaja, A. Kuzmin, O. Shardt, G. Silva, and E. M. Viggen, *The Lattice Boltzmann Method* (Springer, New York, 2017).
[75] I. Ginzburg, F. Verhaeghe, and D. d'Humieres, Two-relaxation-time lattice Boltzmann scheme: About parametrization, velocity, pressure and mixed boundary conditions, Commun. Comput. Phys. **3**, 427 (2008).
[76] S. Khirevich, I. Ginzburg, and U. Tallarek, Coarse-and fine-grid numerical behavior of MRT/TRT lattice-Boltzmann schemes in regular and random sphere packings, J. Comput. Phys. **281**, 708 (2015).
[77] I. Ginzburg, L. Roux, and G. Silva, Local boundary reflections in lattice Boltzmann schemes: Spurious boundary layers and their impact on the velocity, diffusion and dispersion, C. R. Méc. **343**, 518 (2015).
[78] I. Ginzburg, Prediction of the moments in advection-diffusion lattice Boltzmann method. II. Attenuation of the boundary layers via double-Λ bounce-back flux scheme, Phys. Rev. E **95**, 013305 (2017).

[79] Y. Guan, J. Riley, and I. Novosselov, Three-dimensional electro-convective vortices in cross-flow, arXiv:1908.03861.
[80] H. Müller, M. Lücke, and M. Kamps, Transversal convection patterns in horizontal shear flow, Phys. Rev. A **45**, 3714 (1992).
[81] H. Müller, M. Lücke, and M. Kamps, Convective patterns in horizontal flow, Europhys. Lett. **10**, 451 (1989).
[82] H. Müller, M. Tveitereid, and S. Trainoff, Rayleigh-Bénard problem with imposed weak through-flow: Two coupled Ginzburg-Landau equations, Phys. Rev. E **48**, 263 (1993).
[83] M. Tveitereid and H. W. Müller, Pattern selection at the onset of Rayleigh-Bénard convection in a horizontal shear flow, Phys. Rev. E **50**, 1219 (1994).
[84] IEEE-DEIS-EHD Technical Committee, Recommended international standard for dimensionless parameters used in electrohydrodynamics, IEEE Trans. Dielectr. Electr. Insul. **10**, 3 (2003).
[85] J.-S. Chang, A. J. Kelly, and J. M. Crowley, *Handbook of Electrostatic Processes* (CRC Press, Boca Raton, FL, 1995).

Correction: Equations (6), (7), (11), (12), (17), and (18) and the last lines of the captions to Figs. 1 and 6 contained minor errors and have been fixed. Two minor production errors were found in Sec. III and have been rectified.